This is the accepted version of this journal article:

Melchels, Ferry P.W. and Bertoldi, Katia and Gabbrielli, Ruggero and Velders, Aldrik and Feijen, Jan and Grijpma, Dirk W. (2010) *Mathematically defined tissue engineering scaffold architectures prepared by stereolithography.* Biomaterials, 31(27). pp. 6909-6916.

Mathematically defined tissue engineering scaffold architectures prepared by stereolithography

Ferry Melchels[1], Katia Bertoldi[2], Ruggero Gabbrielli[3], Aldrik Velders[4], Jan Feijen[1] and Dirk Grijpma[1,5,*]

keywords: rapid prototyping; stereolithography; microstructure; tissue engineering scaffold; three dimensional printing

[1] MIRA Institute for Biomedical Technology and Technical Medicine, Department of Polymer Chemistry and Biomaterials, University of Twente, P.O. Box 217, 7500 AE, Enschede, The Netherlands
[2] Department of Multi Scale Mechanics, University of Twente, P.O. Box 217, 7500 AE, Enschede, The Netherlands
[3] School of Engineering, Swansea University, SA2 8PP, Swansea, United Kingdom
[4] MESA+ Institute for Nanotechnology, University of Twente, P.O. Box 217, 7500 AE, Enschede, The Netherlands
[5] Department of Biomedical Engineering, University Medical Centre Groningen and University of Groningen, PO Box 196, 9700 AD, Groningen, The Netherlands

[*] e-mail: d.w.grijpma@tnw.utwente.nl; tel. +31 53 489 2966; fax. +31 53 489 2155

Abstract

The technology employed for the preparation of tissue engineering scaffolds restricts the materials choice and the extent to which the architecture can be designed. Here we show the versatility of stereolithography with respect to materials and freedom of design. Porous scaffolds are designed with computer software and built with either a poly(D,L-lactide)-based resin or a poly(D,L-lactide-*co*-ε-caprolactone)-based resin. Characterisation of the scaffolds by micro computed tomography shows excellent reproduction of the designs. The mechanical properties are evaluated in compression, and show good agreement with finite element predictions. The mechanical properties of scaffolds can be controlled by the combination of material and scaffold pore architecture. The presented technology and materials enable an accurate preparation of tissue engineering scaffolds with a large freedom of design, and properties ranging from rigid and strong to highly flexible and elastic.

Introduction

The preparation of porous structures on the micron-level with full freedom of design is still a challenge. One application is in tissue engineering, where porous biodegradable structures serve as temporary supports for the regeneration of tissue [1]. Such scaffolds should comply with the surrounding native tissue, which imposes requirements on properties such as stiffness, strength, biocompatibility and biodegradability [2]. Besides the properties of the material, also the pore architecture of a scaffold is of great influence on its functionality. The architecture influences mechanical properties, cell adhesion and proliferation, transport phenomena and degradation behaviour.

Conventional scaffold fabrication techniques such as salt-leaching, gas-foaming and phase-separation followed by freeze-drying, allow the tuning of only a few parameters like porosity and pore size [3]. Advances in rapid prototyping techniques have significantly improved the control over the whole design of three-dimensional (3d) solid and porous structures [4, 5]. Among these techniques are selective laser sintering [5, 6], fused deposition modelling (or 3d fibber plotting) [7], 3d printing [8] and stereolithography [9]. The latter is particularly versatile with respect to the freedom of design and scale: sub-micron structures [10] to decimetre-sized objects [11] can be built. The working principle of stereolithography is based on spatially controlled solidification of a liquid photo-polymerisable resin. Using a computer-controlled laser beam or digital light projection, and a computer-driven support platform, a 3d object can be constructed in a layer-by-layer fashion. Structural parameters such as porosity and pore size, and even gradients thereof, can be freely varied. While by using fibber plotting methods little variation in patterning of structures is possible,

and laser sintering is limited by the need to process small and monodisperse particles of semi-crystalline polymers, stereolithography requires a photo-sensitive polymer formulation. The availability of suitable resins is very limited, which in general leads to non-degradable addition-type polymer networks.

When fabricating medical implants such as tissue engineering scaffolds, biodegradability is essential. A degradable photo-polymerisable system can be obtained by chain-crosslinking hydrolysable oligomers with reactive end-groups [12, 13]. For example, poly(D,L-lactide) (PDLLA) functionalised with methacrylate groups can be crosslinked to form rigid polymer networks [14]. With values of the elasticity modulus of approximately 3 GPa, poly(D,L-lactide) polymers are one of the few biodegradable polymers with mechanical properties that approach those of bone (the E-modulus of bone is 3 to 30 GPa [3]). They have been applied in resorbable bone fixation devices clinically and for use in bone tissue engineering. The ring opening polymerisation of cyclic esters (lactones) and cyclic carbonates is very versatile, and allows the preparation of oligomers and macromers of a wide variety of resorbable materials. Introducing -caprolactone (CL) by co-polymerisation reduces the glass transition temperature and flexible rubber-like networks are obtained [15]. Copolymers of lactide and caprolactone have successfully been applied in tissue engineering as well [16]. In this paper we will show how to design biodegradable porous structures with refined architectures and prepare these by stereolithography at high resolution. Also, we will show in which ways the mechanical properties of these scaffolds can be tailored.

Materials and Methods

Design of porous architectures

The cube architecture was designed using Rhinoceros 4.0 CAD software (McNeel). Starting from a solid cube measuring 830x830x830 μm^3, a porous construct was obtained by removal of rectangular beams with cross-sections of 530x530 μm^2 in the three directions. This results in a cubic unit cell with 150 μm thick struts and a porosity of 70%. K3DSurf v0.6.2 software (http://k3dsurf.sourceforge.net) was used to generate CAD-files that describe the surfaces of gyroid (G) and diamond (D) architectures. The following trigonometric functions with boundary conditions x,y=[-6π,6π] and z=[-12π,12π] were used:

G: cos(x)·sin(y) + cos(y)·sin(z) + cos(z)·sin(x) - 0.60 = 0

D: sin(x)·sin(y)·sin(z) + sin(x)·cos(y)·cos(z) + cos(x)·sin(y)·cos(z) + cos(x)·cos(y)·sin(z) − 0.42 = 0

To obtain porous structures with porosities of approximately 70 %, offset values of -0.60 for the gyroid- and -0.42 for the diamond architecture are required. The gradient in pore size and porosity

of the gyroid structure presented was introduced by adding the term -0.032·z to the equation for z-values of [-12π,0]. With this linear term, the porosity is designed to gradually decrease from 70 % at the mid-section to 30 % at the bottom end of the structure. Rhinoceros software was used to scale the CAD-files of all three architectures to the desired dimensions. The 5x5x10 mm³ designs were scaled-up by a factor 1.28, anticipating the shrinkage upon extraction of non-reactive diluent from the built structures. Envisiontec Perfactory RP2.0 software was used to slice the 3D CAD-files. The stack of bitmaps generated, is the input for the layer-by-layer building process.

Macromer synthesis

Hydroxyl-terminated oligomers were synthesised by ring-opening polymerisation (130 °C, 40 h) of D,L-lactide (DLLA, Purac Biochem) using 1,6-hexanediol (Sigma-Aldrich) as initiator and stannous octoate (Sigma-Aldrich) as catalyst. P(DLLA-*co*-CL) oligomers were synthesised in a similar way, using an equimolar mixture of D,L-lactide and ε-caprolactone (CL, Sigma-Aldrich). The monomer-to-initiator ratio was adjusted to yield oligomers with a molecular weight of 5 kg·mol^{-1} (molecular weights were confirmed by ^{1}H-NMR analysis). The termini of the oligomers were reacted with methacrylic anhydride (Sigma-Aldrich) in the presence of triethyl amine (Sigma-Aldrich) (both in a 20 mol % excess) in dried dichloromethane for 5 d to yield methacrylate end-functionalised lactide macromers. After precipitation from isopropanol, washing with water and freeze-drying, pure macromers with a degree of functionalisation of 92-99 % (determined by ^{1}H-NMR analysis) were obtained.

Fabrication of porous structures

The resins used for stereolithography consisted of 58 wt% PDLLA macromer, 40 wt% dry N-methylpyrrolidone (NMP, Fluka) as a non-reactive diluent, 2 wt% ethyl-2,4,6-trimethylbenzoylphenylphosphinate (Lucirin TPO-L photo-initiator from BASF), 0.2 wt% Orasol Orange G dye (Ciba SC) and 0.1 wt% α-tocopherol inhibitor (Fluka). A commercial stereolithography apparatus (Envisiontec Perfactory Mini Multilens SLA) was employed to build designed structures. The building process involves subsequent projections of 1280x1024 pixels, each 32x32 μm² in size. Layers with a thickness of 25 μm were cured by irradiating for 30 s with blue light (intensity 16 mW·cm^{-2}). Uncured excess resin was washed out and the diluent, non-reacted macromer and photo-initiator were extracted from the structures with acetone. The extracted structures were then dried at 90 °C for 2 d under a nitrogen flow.

A similar resin, containing camphorquinone instead of Lucirin TPO-L and chloroform instead of NMP, was used to prepare porous structures by a salt-leaching process. This resin did not contain a dye. The resin was mixed with NaCl particles sieved to sizes of 425-710 μm, brought into tubular

polypropylene moulds (inner diameter 14 mm) and cured by irradiation through the tube wall with a Kerr dental light (mono-chromatic blue LED light, wavelength 470 nm, intensity 1000 mW·cm^{-2}) for 40 s. The specimens were frozen in liquid nitrogen, cut to the desired dimensions, and post-cured by heating to 90 °C for 12 hrs. The salt-containing composites were extracted in acetone for 2 d, and the salt fraction was leached out with water during a period of 7 d. Then, the porous structures were dried at 90 °C for 2 d under a nitrogen flow.

Analyses of the porous structures

Structural analysis was performed by micro-computed tomography (µCT) using a GE eXplore Locus SP scanner (General Electric) at 14.3 µm resolution. Scanning was done at an X-ray tube voltage of 80 kV, a current of 80 µA and an exposure time of 3000 ms. No filter was applied. After reconstruction using the Feldkamp algorithm, thresholded isosurface images were obtained (GE MicroView software). The software was also used to generate pore size distribution maps of the structures. In these 3D matrices, size values are assigned to pore voxels. These sizes correspond to the diameter of the largest sphere that can be fitted in the pore space and contains that particular pore voxel. The maps were used to calculate porosities, pore size distributions, pore surface areas and pore accessibility curves (Mathworks Matlab 2008). In determining the porosity gradient curve (**Fig. 4**), the porosity at a particular scaffold height was determined by taking the pore volume fraction of every individual voxel plane. The accessibility of the pore networks was quantified by first thresholding the pore size distribution maps to exclude pores smaller than a certain diameter, then the remaining pore volume fraction connected to the exterior of the structure was determined. This was repeated for a range of diameters. To compare the built structures with the software designs, the latter were evaluated in the same manner as well. For this, the stacks of bitmaps used in the layer-by-layer fabrication of the structures by SLA, were also imported into the µCT analysis software.

To model and predict the mechanical behaviour of structures with different designed pore architectures, numerical simulations were conducted. First the compressive response of solid PDLLA and P(DLLA-*co*-CL) network specimens built by stereolithography was evaluated. Mechanical testing in compression was done using a Zwick Z020 universal tensile tester in a range of compression rates. The bulk properties of each material were described mathematically using a constitutive model. The model was implemented into finite element software code (ABAQUS), which then allowed simulating and predicting the deformation characteristics of the designed porous structures. See Supporting Information for details on the development of the constitutive models and the finite element analysis.

Nuclear magnetic resonance spectroscopy (^{1}H-NMR) was performed on networks swollen in deuterated acetone using a Varian 600 MHz apparatus equipped with a high-resolution probe operating under magic angle spinning (HR-MAS) conditions.

Results and Discussion

Design and fabrication of porous structures

PDLLA and P(DLLA-*co*-CL) dimethacrylate macromers with a molecular weight of 5 kg·mol^{-1} were dissolved in a non-reactive diluent together with other resin components and used in the stereolithography rapid prototyping process. **Fig. 1** gives an overview of the designed and built architectures. Three sophisticated porous architectures were designed: a cube, a diamond, and a gyroid architecture. The cube architecture is an anisotropic lattice-like structure, similar to those that many rapid prototyping methods are restricted to. With the stereolithography technique used here, each layer is built using a distinct pattern of 1.3x10^6 light pixels that can be switched on or off independently. This allows for the fabrication of complex structures such as the diamond and gyroid architectures. Their surfaces are defined by trigonometric implicit functions, where the spatial variables are symmetrically ordered within the trigonometric terms. The functions are triply periodic and are uniquely defined by their unit cell [17]. They closely approximate the minimal surfaces of Schwarz and Schoen [18, 19], of which the mean curvature is zero at every point. Addition of an offset value to these implicit functions allows designing porous structures with diamond or gyroid architectures and specific porosities. The functions employed are presented in the experimental section.
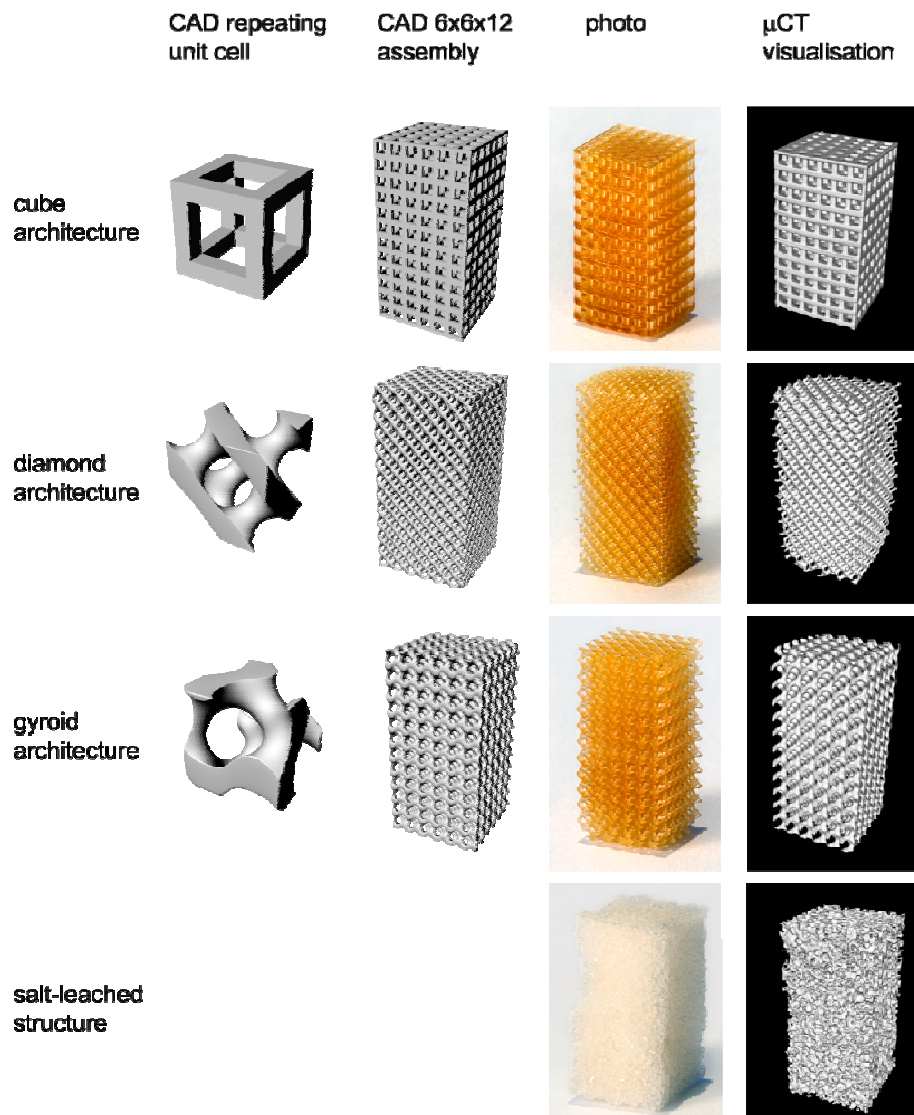
Figure 1. Visualisations of the different porous architectures. Columns: (1) CAD-designs of the repeating unit cells (2) CAD-designs of assemblies of 6x6x12 unit cells (3) photos of the built structures (4) visualisations obtained by μCT-scanning of the built structures. All structures measure approximately 5x5x10 mm.

For the different architectures, space-filling computer models can be generated from assemblies of the respective unit cells. Models consisting of 6x6x12 unit cells were then built by stereolithography using a resin based on PDLLA or P(DLLA-*co*-CL) macromers and a non-reactive diluent. Upon removal of the diluent by extraction and drying, the structures shrink by 22 %. This shrinkage is homogenous and reproducible, and could be compensated for by adjusting the dimensions of the design. Furthermore, to enable precise control over the depth of curing in the layer-by-layer stereolithography fabrication process, a dye is required to attenuate the light intensity. In our setup

photo-polymerisation is induced by blue light, and in the resin an orange dye was used. This determines the colour of the structures built.

For comparison, porous structures with similar average pore sizes and porosities were prepared by a conventional porogen leaching method. Especially salt-leaching is a widely used method to prepare tissue engineering scaffolds. The PDLLA-based resin containing dispersed salt particles with sizes ranging from 425-710 μm was photo-polymerised, and porous structures were obtained upon leaching with water. In this case the presence of dye is not required.

The porous structures were analysed by micro computed tomography (μCT), of which visualisations are shown in the most right column of **Fig. 1**. The μCT images precisely match the designed models of the different architectures. It is clear that the structure prepared by salt leaching is much less regular.

Analyses of built structures

To assess the accuracy of the stereolithography technique, a gyroid scaffold built from the PDLLA material was compared to its computer aided design. The graphical data obtained by μCT scanning was superimposed on the CAD data, enabling both visual and quantifiable comparisons. **Fig. 2** shows merged images of the gyroid design (in grey) and μCT data (in orange) both in three dimensions and in two dimensions. It can be seen that over the whole porous structure the designed and built architectures nearly coincide, indicating a very high accuracy of the technique. In the right of the figure, a cross-section of the μCT data of the built structure is depicted as a semi-transparent overlay over the CAD cross-section, showing exactly where the two match. Except for slight shearing of the built structure in the counter-clockwise direction and some overcure, the computer aided design is very well reproduced. When expressed in pixels, the agreement of the CAD and the μCT images of the built structures is 95 %.

designed and built
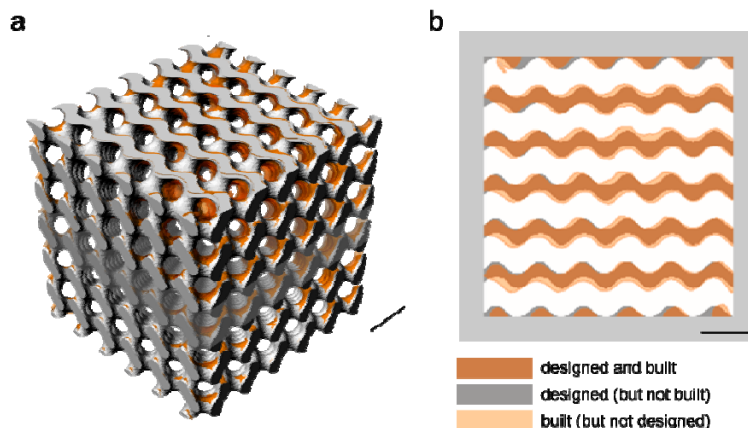designed (but not built)
built (but not designed)

Figure 2. Superimposed 3d image of the gyroid computer aided design (in grey) and the μCT visualisation of the built structure (in orange). b: Semi-transparent overlay of a cross-section of the CAD (grey) and the μCT (orange) data. The overlapping area is shown in dark orange. Scale bars are 1 mm.

From μCT data of built scaffolds, structural parameters such as porosities, pore sizes and specific surface areas (surface area of pores per overall volume) can be assessed. For the different architectures, the determined values are compared to those of the corresponding designs in **Table 1**. The designs were evaluated in the same manner as the built structures. It can be seen that the results match those of the designs well.

Table 1. Comparison of structural parameters of the designed and built porous structures as determined by μCT.

architecture		porosity [vol %]		pore size [μm]		specific surface area [mm^{-1}]	
		design	built[a]	design[b]	built[b]	design	built[a]
cubes	PDLLA	66	64 ± 5	622 ± 164	537 ± 171	3.87	4.44 ± 0.08
diamond	PDLLA	68	68 ± 2	398 ± 57	378 ± 74	6.56	7.10 ± 0.44
	P(DLLA-*co*-CL)		67 ± 3		352 ± 94		7.32 ± 0.55
gyroid	PDLLA	68	69 ± 2	453 ± 55	455 ± 71	5.34	5.33 ± 0.19
	P(DLLA-*co*-CL)		69 ± 3		462 ± 81		5.54 ± 0.16
salt-leached	PDLLA	-	77 ± 7	-	353 ± 143	-	12.4 ± 4.1

[a]: average ± standard deviation (n=3). [b]: volume average ± standard deviation of the pore size distribution (n=3)

Although scaffolds with relatively small pore sizes provide high surface areas for cells to adhere to and to proliferate on, larger pores that allow for vascularisation, tissue ingrowth and adequate nutrient transport are required as well. For *in vivo* bone tissue engineering for example, minimum pore sizes of 300 μm are needed for capillary formation to occur. For larger sizes, several studies revealed no statistical difference in bone ingrowth and bone formation in scaffolds with pores up to 800 μm in size [20]. The stereolithography technique presented here allows for the controlled preparation of scaffolds with pore sizes in the optimal range for (bone) tissue engineering.

The pore size distributions of the built gyroid design and the prepared salt-leached structure, which is a typical scaffold used in tissue engineering, are compared and depicted in **Fig. 3**. The data is

visualised as an indexed colour-map and quantitatively presented as a histogram. The relatively narrow pore size distribution of the built gyroid structure results in a very even colouring in the indexed colour maps. These pore size distribution maps can also be used to assess the interconnectivity of the pores in a quantitative manner. Using an algorithm that mimics mercury porosimetry, the permeation of spheres of different diameters through the pore network is simulated. For a given sphere size, this simulation will allow to determine the volume of pores that is accessible for that sphere. This therefore represents the fraction of the pore volume that is connected to the exterior of the scaffold by channels with diameters larger than that sphere.
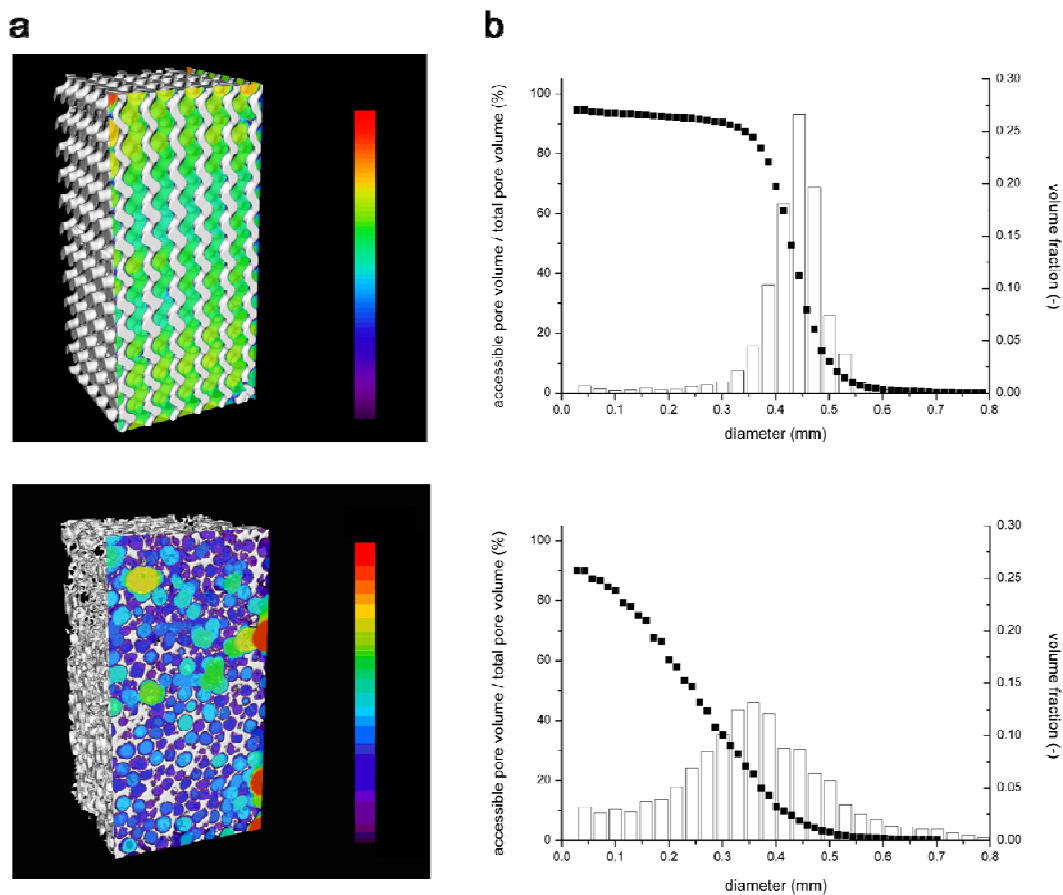

Figure 3. Pore size distributions and accessibility curves of built PDLLA gyroid structures and salt-leached scaffolds from μCT analyses. a: Pore size distribution maps with pore sizes indicated by a colour scale. b: The bars in the histogram correspond to volume fractions of pores with specific diameters. The curves represent the pore volume that is accessible for permeating spheres of different diameters in a simulation.

These resulting accessibility curves are also depicted in **Fig. 3**. Here too, clear differences between the gyroid construct and the salt-leached structure can be observed. The built gyroid structure shows a very steep decrease in accessibility at pore sizes close to the average pore size value, whereas accessibility of pores in the salt-leached scaffold decreases gradually already from pore sizes much smaller than the average size. This implies that the interconnections between the pores are much smaller than the pores themselves. In contrast, the pore space throughout the gyroid structure consists of channels with approximately equal diameters. This leads to the high accessibility observed for spheres with diameters up to the average pore size. The resulting high permeability ensures good transport properties, which is important in tissue engineering.

Mechanical properties of porous structures

The influence of the pore architecture on the mechanical properties of the structures was analysed as well. **Fig. 4a** compares the compressive response of porous PDLLA structures with cubic and gyroid pore architectures at similar porosity (approximately 67 %). In the porous structures with cube architecture, a high stiffness is observed as result of the alignment of the vertical struts with the compressive force. The Young's modulus is 324±39 MPa for structures with a porosity of 64±5 %. The gyroid architecture is characterised by curved surfaces; these porous structures exhibit less rigid behaviour (169±21 MPa at 69±2 % porosity).
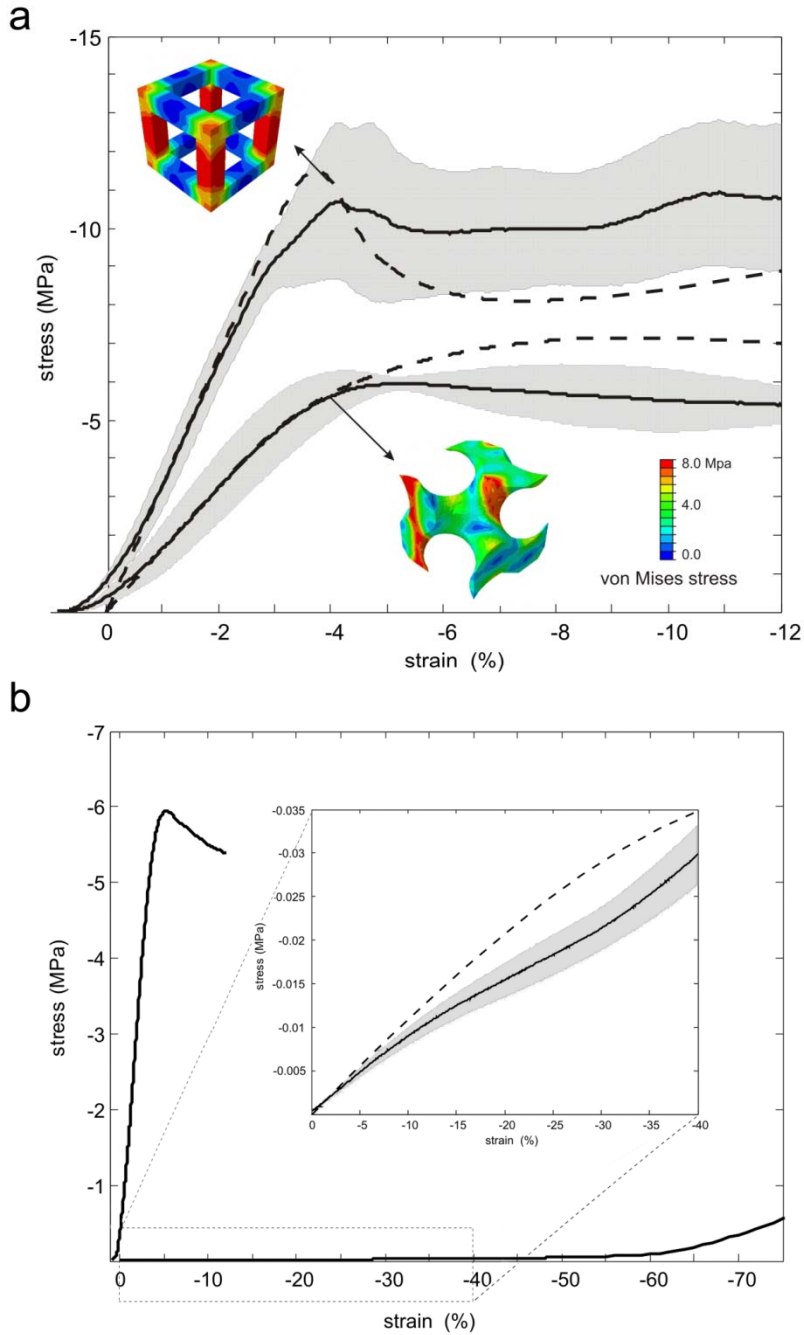
Figure 4. Compression stress-strain diagrams of built structures and simulations. a: Stress-strain diagrams of PDLLA structures with cube and gyroid architectures, at similar porosity. The experimental data are depicted as average (solid line) ± standard deviation (shaded area) of 5 samples and compared to the curve predicted by finite element analysis (dashed line). The inserted CAD unit cells show the von Mises stress distribution at a simulated 4% macroscopic strain. b: Compression stress-strain diagrams of gyroid structures built from rigid PDLLA and flexible P(DLLA-*co*-CL) at similar porosity. The insert

presents the experimental data of the flexible gyroid structures as average (solid line) ± standard deviation (shaded area) of 5 samples and the curve predicted by finite element simulation (dashed line).

Finite element simulations of the compression experiments were conducted using the different CAD unit cells. For this, the stress-strain responses of bulk PDLLA and P(DLLA-*co*-CL) were first determined using solid specimens that were also fabricated from the resins by stereolithography. Two different constitutive models were then used to capture the experimentally observed behaviour and were implemented into a finite element software code (see **Supporting Information**). Direct comparison shows excellent agreement between the model predictions and the experimental results. As numerical analyses allow us to predict the mechanical behaviour of porous structures *a priori*, it is now possible to optimise scaffold designs with respect to their mechanical properties.

The figure also shows that for gyroid architectures, stress and strain are much more homogeneously distributed throughout the structure than for cube architectures. A tissue engineering scaffold with gyroid architecture will expose adhering cells to more equal mechanical stimuli throughout the structure. As cells respond to deformation of the matrix to which they adhere [21], this could be beneficial.

Compression data of gyroid structures of similar porosity built from rigid PDLLA and from flexible P(DLLA-*co*-CL) are shown in **Fig. 4b**. The difference in the bulk elastic modulus of the different polymer networks (respectively 2.5×10^3 and 2 MPa) is reflected in the global stiffness of the approximately 70% porous structures (respectively 165 and 0.12 MPa). The structures show markedly distinct mechanical behaviour: while the PDLLA gyroid structures yield plastically at approximately 5 % strain and 6 MPa stress, a same structure built from the copolymer can be reversibly deformed up to 70 % strain and 0.43 MPa stress with little hysteresis. The mechanical behaviour of the latter structures was unaffected for at least 1000 cycles (**Fig. 5**). Intermediate mechanical properties can be obtained by adjusting the copolymer composition, allowing for the preparation of designed structures that are suitable for the engineering of a wide range of tissues.
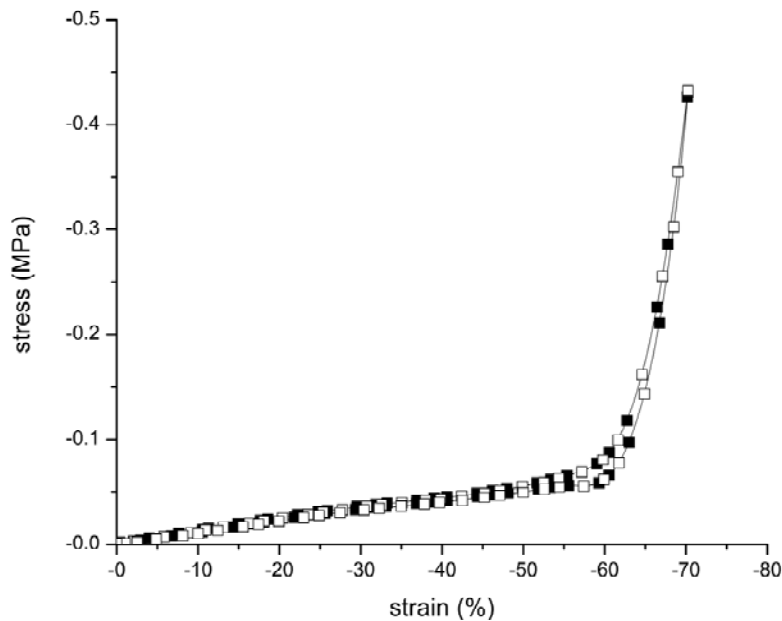
Figure 5. Overlay of stress-strain diagrams from cyclic compression (loading-unloading with a strain rate of 30 %·min^{-1}) of a 69 % porous P(DLLA-*co*-CL) gyroid structure. Cycle 1, 100 and 1000 are depicted.

Mathematically defined tissue engineering scaffolds

Ordered porous structures such as the built gyroid and diamond architectures, are envisaged to be very well suited for use as scaffolds in tissue engineering [22]. The good accessibility of pores and resulting high permeability of the scaffold will facilitate the seeding of cells [23] and the transport of nutrients and metabolites, either during in vitro culture or after implantation in the body. Furthermore, scaffold morphology is a key factor determining tissue formation, as the pore network initially provides the spatial template for cell adhesion and proliferation and the deposition of extra-cellular matrix [24].

In specific cases, scaffolds with defined but non-uniform characteristics are desired. Bone tissue for example, varies spatially in structure and composition. In load-bearing bone, the properties of the tissue progressively vary from those of cortical bone to those of trabecular bone. In the engineering of other tissues, optimal conditions for cell culturing can differ from those of bone. To repair osteochondral defects, tissue constructs comprising both bone and cartilage are to be engineered [25]. For this, structures in which gradients of properties such as permeability and stiffness exist are desired [26].

A gradient in size and volume fraction of the pores can be introduced by adding a linear term to the mathematical equation used to describe the pore architecture [27]. To part of the design of a scaffold with gyroid pore architecture, such a term was added. The scaffold was then built by stereolithography using the PDLLA-based resin. **Fig. 6** shows a μCT-visualisation of the resulting scaffold. It is clear that the top half of the structure is much more open than the bottom part, where a gradient in pore size and porosity can be seen. The right part of the figure is a quantification of the average porosity as a function of the height of the scaffold, as determined by μCT. These results are compared to the original design. The graph shows that the porosity gradually decreases from the middle of the structure downwards. This gradient in porosity and pore size will result in a stiffness and permeability gradient as well.
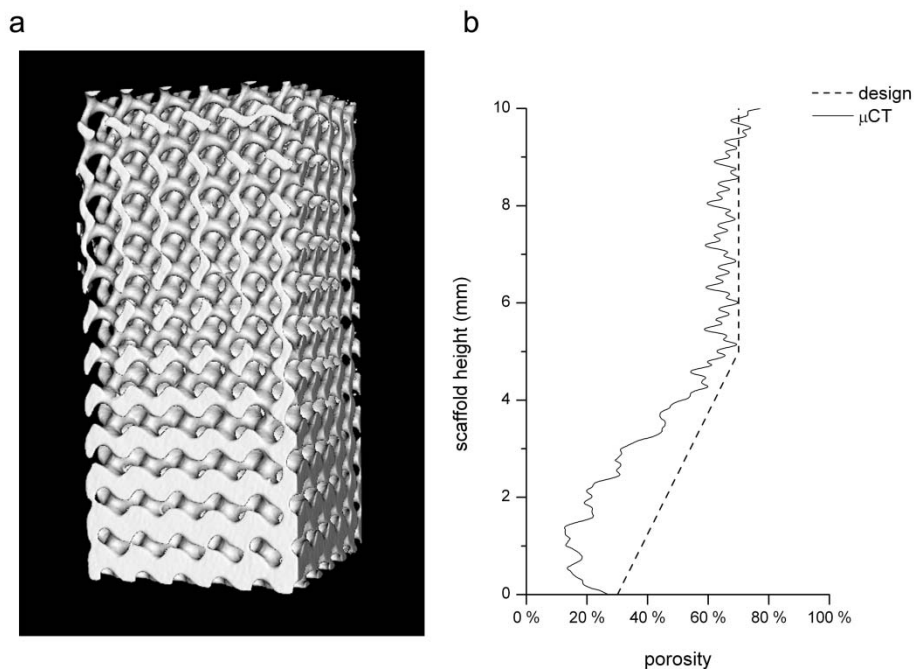

Figure 6. Built PDLLA scaffold with gyroid architecture showing a gradient in porosity and pore size. a: μCT visualisation. b: Change in the average porosity with scaffold height (solid line) in comparison with the designed porosity (dotted line).

The overall porosity of the built structure is somewhat lower than designed. This was also the case for the isotropic gyroid structures presented in **Fig. 2**. It is likely that local warming up of the resin due to the intensity of the light and the exothermic polymerisation reaction has resulted in overcure. At lower porosities the absorbed energy per volume is relatively high, and deviation from the design

is more pronounced. **Fig. 6** also shows that the effect of overcure is minimal at the boundaries of the structure, where heat can be exchanged with the surrounding non-illuminated resin.

In the photo-initiated polymerisation in stereolithography, the conversion of reactive end groups is incomplete. After swelling the polymer networks in deuterated acetone, conversions of 85 to 95 % could be determined by high-resolution NMR spectroscopy (see **Fig. 7** for an example spectrum). The unreacted double bonds remain available for subsequent covalent functionalisation. These can be used, for example, to adjust the hydrophilicity of the networks or to immobilise cell-adhesive peptides at the surfaces of the porous structures [28].
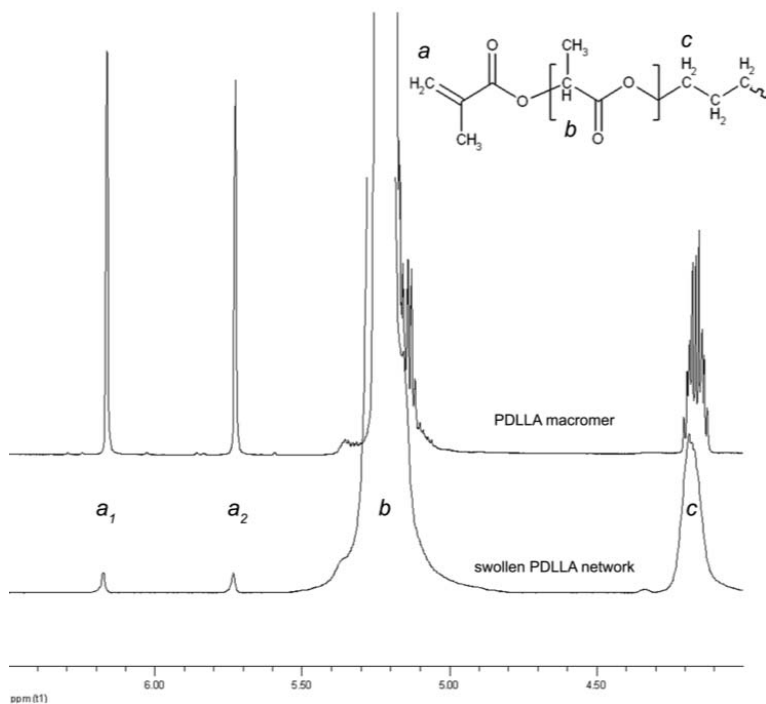

Figure 7. ¹H-NMR spectra (600 MHz) of a PDLLA macromer and network with acetone-d₆ as solvent or swelling agent. High-resolution spectra of networks were obtained under magic angle spinning conditions. Here, peaks a₁ and a₂ correspond to the vinyl protons of unreacted methacrylate groups in the network.

Although we demonstrated here the suitability of the stereolithography technique for the preparation of tissue engineering scaffolds, mathematically defined porous structures can be useful in many other applications as well. Tight control over the pore size distribution can lead to materials with photonic band gap properties [29], thermal, acoustic or electrical insulating characteristics, or to mechanical materials that exhibit negative Poisson ratios [30].

Conclusions

We have shown that stereolithography fabrication methods can be used to accurately prepare tissue engineering scaffolds with designs that can be modelled, allowing optimisation of the properties of the structures. By varying the composition of the macromers and the pore architecture, scaffolds with a large range of mechanical properties can be obtained.

Acknowledgements

References

[1]   Freed LE, Vunjak-Novakovic G, Biron RJ, Eagles DB, Lesnoy DC, Barlow SK, et al. Biodegradable polymer scaffolds for tissue engineering. Bio-Technol. 1994;12(7):689-693.
[2]   Hutmacher DW. Scaffolds in tissue engineering bone and cartilage. Biomaterials. 2000;21(24):2529-2543.
[3]   Yang SF, Leong KF, Du ZH, Chua CK. The design of scaffolds for use in tissue engineering. Part 1. Traditional factors. Tissue Eng. 2001;7(6):679-689.
[4]   Hollister SJ. Porous scaffold design for tissue engineering. Nat Mater. 2005;4(7):518-524.
[5]   Antonov EN, Bagratashvili VN, Whitaker MJ, Barry JJA, Shakesheff KM, Konovalov AN, et al. Three-dimensional bioactive and biodegradable scaffolds fabricated by surface-selective laser sintering. Adv Mater. 2005;17(3):327-+.
[6]   Williams JM, Adewunmi A, Schek RM, Flanagan CL, Krebsbach PH, Feinberg SE, et al. Bone tissue engineering using polycaprolactone scaffolds fabricated via selective laser sintering. Biomaterials. 2005;26(23):4817-4827.
[7]   Hutmacher DW, Schantz T, Zein I, Ng KW, Teoh SH, Tan KC. Mechanical properties and cell cultural response of polycaprolactone scaffolds designed and fabricated via fused deposition modeling. J Biomed Mater Res. 2001;55(2):203-216.
[8]   Giordano RA, Wu BM, Borland SW, Cima LG, Sachs EM, Cima MJ. Mechanical properties of dense polylactic acid structures fabricated by three dimensional printing. J Biomat Sci-Polym E. 1996;8(1):63-75.
[9]   Cooke MN, Fisher JP, Dean D, Rimnac C, Mikos AG. Use of stereolithography to manufacture critical-sized 3D biodegradable scaffolds for bone ingrowth. J Biomed Mater Res B Appl Biomater. 2003;64B(2):65-69.
[10]   Maruo S, Ikuta K. Submicron stereolithography for the production of freely movable mechanisms by using single-photon polymerization. Sens Actuators A Phys. 2002;100(1):70-76.
[11]   Klein HM, Schneider W, Nawrath J, Gernot T, Voy ED, Krasny R. Stereolithography model construction based on 3-dimensional reconstructions according to CAM. Rofo Fortschr Rontg. 1992;156(5):429-432.
[12]   Sawhney AS, Pathak CP, Hubbell JA. Bioerodible hydrogels based on photopolymerized poly(ethylene glycol)-co-poly(alpha-hydroxy acid) diacrylate macromers. Macromolecules. 1993;26(4):581-587.
[13]   Ericsson J, Hult A. Novel degradable methacrylate-based and para-vinylphenoxy-based oligomers .1. synthesis and characterization. Makromol Chem. 1991;192(7):1609-1619.
[14]   Storey RF, Warren SC, Allison CJ, Wiggins JS, Puckett AD. Synthesis of bioabsorbable networks from methacrylate-endcapped polyesters. Polymer. 1993;34(20):4365-4372.
[15]   Helminen AO, Korhonen H, Seppala JV. Cross-linked poly(epsilon-caprolactone/D,L-lactide) copolymers with elastic properties. Macromol Chem Phys. 2002;203(18):2630-2639.
[16]   Matsubayashi K, Fedak PWM, Mickle DAG, Weisel RD, Ozawa T, Li RK. Improved left ventricular aneurysm repair with bioengineered vascular smooth muscle grafts. Circulation. 2003;108(10):219-225.
[17]   Vonschnering HG, Nesper R. Nodal surfaces of Fourier-series - fundamental invariants of structured matter. Z Phys B Con Mat. 1991;83(3):407-412.
[18]   Schwarz HA. Gesammelte mathematische Abhandlungen. Berlin: Springer-Verlag; 1890.
[19]   Schoen AH. Infinite periodic minimal surfaces without self-intersections. Nasa Technical Note 5541. Springfield: Clearinghouse for Federal Scientific and Technical Information; 1970.

[20]   Karageorgiou V, Kaplan D. Porosity of 3D biomaterial scaffolds and osteogenesis. Biomaterials. 2005;26(27):5474-5491.

[21]   Bao G, Suresh S. Cell and molecular mechanics of biological materials. Nat Mater. 2003;2(11):715-725.

[22]   Rajagopalan S, Robb RA. Schwarz meets Schwann: Design and fabrication of biomorphic and durataxic tissue engineering scaffolds. Med Image Anal. 2006;10(5):693-712.

[23]   Figallo E, Flaibani M, Zavan B, Abatangelo G, Elvassore N. Micropatterned biopolymer 3D scaffold for static and dynamic culture of human fibroblasts. Biotechnol Prog. 2007;23(1):210-216.

[24]   Wang HJ, Pieper J, Peters F, van Blitterswijk CA, Lamme EN. Synthetic scaffold morphology controls human dermal connective tissue formation. J Biomed Mater Res. 2005;74A(4):523-532.

[25]   Martin I, Miot S, Barbero A, Jakob M, Wendt D. Osteochondral tissue engineering. J Biomech. 2007;40(4):750-765.

[26]   Kelly DJ, Prendergast PJ. Prediction of the optimal mechanical properties for a scaffold used in osteochondral defect repair. Tissue Eng. 2006;12(9):2509-2519.

[27]   Gabbrielli R, Turner IG, Bowen CR. Development of modelling methods for materials to be used as bone substitutes. Key Eng Mat. 2008;361-363 II:901-906.

[28]   Drumheller PD, Hubbell JA. Polymer networks with grafted cell-adhesion peptides for highly biospecific cell adhesive substrates. Anal Biochem. 1994;222(2):380-388.

[29]   Man WN, Megens M, Steinhardt PJ, Chaikin PM. Experimental measurement of the photonic properties of icosahedral quasicrystals. Nature. 2005;436(7053):993-996.

[30]   Lakes R. Foam structures with a negative Poissons ratio. Science. 1987;235(4792):1038-1040.

Supporting Information: Constitutive models for polymer networks and numerical analysis

1. Constitutive model for crosslinked poly(D,L-lactide) (PDLLA)

1.1 Experimental results

Uniaxial compression tests were conducted to characterise the material response of PDLLA. Cylindrical specimens were subjected to uniaxial compression at a constant nominal strain rate of 0.1, 0.01, 0.001 and 0.0001 s^{-1} using a Zwick Z020 screw-driven testing machine and the results are shown in **Figure S1**. The tests show that the material exhibits a rate-dependent behaviour, characterised by an initial elastic response, followed by yield, strain softening and strain hardening. The yield point is found to decrease with a decrease in strain rate.
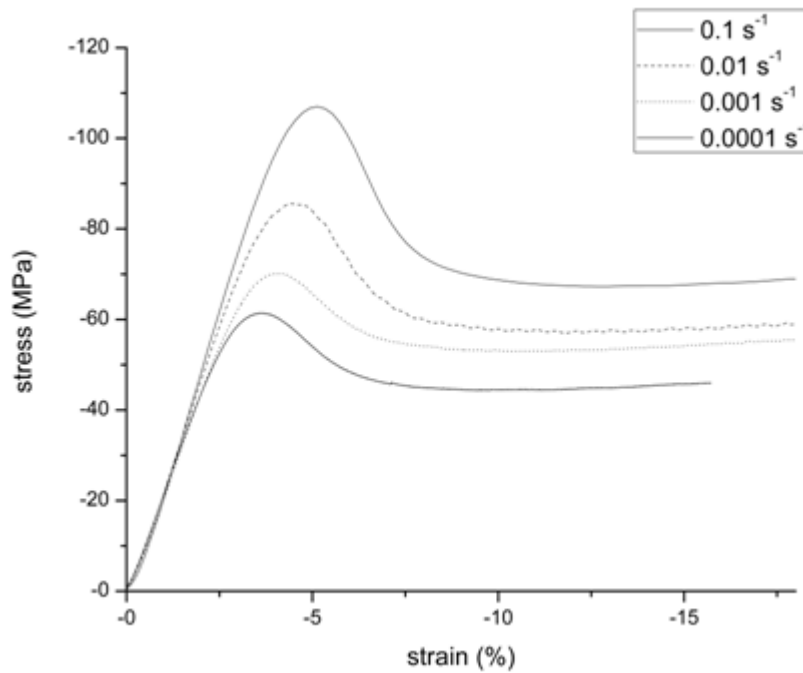

Figure S1. Experimental uniaxial compression stress-strain curves for PDLLA over four decades of strain rate from -0.1 to -0.001 s^{-1}.

1.2 Constitutive model

Following Boyce et al. [1] and using the finite strain kinematics framework of Bergstrom and Boyce [2] a two-mechanism thermo-mechanical constitutive model is used to capture the stress-strain behaviour of the material. Mechanism N represents the resistance due to stretching and orientation of the molecular network, and mechanism V represents the

resistance to intermolecular interaction. Thus, the total stress acting on the material is given by the sum of the stress contributions from the two mechanisms:

$$\sigma = \sigma_N + \sigma_V.$$

1.2.1. Constitutive relations for Mechanism N

Mechanism N is modelled using an 8-chain network model as proposed by Arruda and Boyce [3], so that the Cauchy stress is given by

$$\sigma_N = \frac{\mu}{J} \frac{\sqrt{N}}{\lambda_{chain}} L^{-1}\left(\frac{\lambda_{chain}}{\sqrt{N}}\right) \mathbf{B'},$$

where $\mathbf{B'}$ is the deviatory part of the left Cauchy-Green tensor $\mathbf{B} = \mathbf{FF}^T$ ($\mathbf{F} = \partial \mathbf{x} / \partial \mathbf{X}$ being the total deformation gradient that maps a material point from the reference position $\mathbf{X}$ to its current location $\mathbf{x}$), J=det($\mathbf{F}$), $\lambda_{chain} = \sqrt{\dfrac{tr\mathbf{B}}{3}}$ maps the macroscopic deformation to an average chain stretch and L is the Langevin function defined as $L(\beta) = \coth \beta - \dfrac{1}{\beta}$. The shear modulus and the limiting chain extensibility are denoted by μ and $\sqrt{N}$, respectively.

1.2.2 Constitutive relations for Mechanism V

The deformation gradient $\mathbf{F}$ is then decomposed into elastic and plastic contributions $\mathbf{F} = \mathbf{F}^E \mathbf{F}^P$ and the Cauchy stress σ_V is calculated using $\mathbf{F}_V^E$ as

$$\sigma_V = \frac{1}{\det \mathbf{F}^E}\left(\underline{\mathbf{L}}^E \left(\ln \mathbf{V}^E \right) - \frac{p}{3} \mathbf{I} \right),$$

where $\mathbf{V}^E = \mathbf{F}^E \mathbf{R}^E$ ($\mathbf{R}^E$ being a rotation tensor) and $\underline{\mathbf{L}}^E$ is the fourth order isotropic elasticity tensor

$$\underline{\mathbf{L}}^E = \frac{E}{1+\nu} \mathbf{I}^4 + \frac{E\nu}{(1+\nu)(1-2\nu)} \mathbf{I} \otimes \mathbf{I},$$

G and λ being the Lame constants, $\mathbf{I}^4$ the fourth order identity tensor and $\mathbf{I}$ the second order identity tensor.

The evolution of $\mathbf{F}^E$ is then determined considering the composition of the spatial velocity gradient

$$\mathbf{L} = \dot{\mathbf{F}}\,\mathbf{F} = \dot{\mathbf{F}}^{E}\mathbf{F}^{E\text{-}1} + \mathbf{F}^{E}\mathbf{L}^{P}\mathbf{F}^{E\text{-}1},$$

where $\mathbf{L}^{P}$ can be further decomposed into

$$\mathbf{L}^{P} = \dot{\mathbf{F}}^{P}\mathbf{F}^{P\text{-}1} = \mathbf{D}^{P} + \mathbf{W}^{P}.$$

Without losing generality we can assume $\mathbf{W}^{P} = 0$, whereas the viscoplastic stretch rate $\mathbf{D}^{P}$ is constitutively prescribed to be

$$\mathbf{D}^{P} = \frac{\dot{\gamma}_{V}^{P}}{\sqrt{2}\tau}\boldsymbol{\sigma}_{V}',$$

where $\boldsymbol{\sigma}_{V}'$ denotes the deviatory part of $\boldsymbol{\sigma}_{V}$ and τ is the equivalent shear stress defined as

$$\tau = \sqrt{\frac{1}{2}\boldsymbol{\sigma}_{V}' \bullet \boldsymbol{\sigma}_{V}'}.$$

The viscoplastic shear strain rate $\dot{\gamma}_{V}$ is then constitutively prescribed as

$$\dot{\gamma}_{V} = \dot{\gamma}_{0}\exp\left(\frac{-\Delta G}{k\theta}\left(1 - \frac{\tau}{s - \alpha p}\right)\right) - \dot{\gamma}_{0}\exp\left(\frac{-\Delta G}{k\theta}\left(1 + \frac{\tau}{s - \alpha p}\right)\right),$$

where $\dot{\gamma}_{0}$ is the pre-exponential factor, ΔG is the activation energy, s is the athermal shear strength, θ is the absolute temperature, p is the pressure and α is the pressure coefficient. Further, the evolution rule for s is defined as

$$\dot{s} = h_{0}\left(1 - \frac{s}{s_{s}}\right)\dot{\gamma}_{V},$$

with the initial condition s = s_{0} when $\dot{\gamma}_{V} = 0$.

1.3 Material parameters

The PDLLA model parameters determined by curve fitting are listed in **Table S1**.

Table S1. PDLLA model parameters.

Mechanism V								Mechanism N	
E [MPa]	ν	$\dot{\gamma}_{0}$ [10^{3}s^{-1}]	ΔG [10^{-19}J]	s_{0} [MPa]	s_{s} [MPa]	h_{0} [MPa]	α	N	μ [MPa]
2100	0.33	1.58	1.05	90.73	30	350	0.075	2.4	22

1.4 Model predictions

Figure S2 reports the experimentally observed rate-dependent behaviour for PDLLA under uniaxial compression along with the model simulations of these test conditions. The constitutive model is found to accurately predict the strain rate dependence of the material behaviour during uniaxial compression at low strain rates. The values of the model parameters required used in the simulations are listed in Table S1.
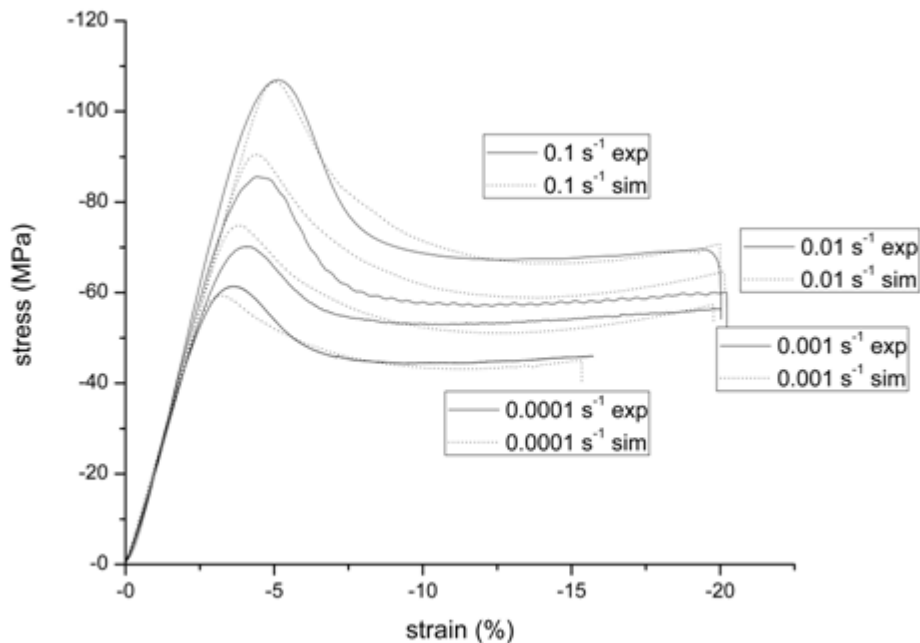

Figure S2. Nominal stress–nominal strain behaviour in uniaxial compression at low strain rates: experimental results (continuous lines) and model predictions (dashed lines).

2. Constitutive model for crosslinked poly(D,L-lactide-co-caprolactone) P(DLLA-co-CL)

2.1 Experimental Results

Uniaxial compression and tension tests were conducted to characterise the material response of P(DLLA-*co*-CL). Cylindrical specimens were subjected to uniaxial compression at a constant nominal strain rate of 0.1, 0.01, 0.001 and 0.0001 s^{-1} using Zwick Z020 screw-driven testing machine. The tests show that the material exhibits behaviour typical for elastomers: large strain elastic behaviour with negligible rate dependence and negligible hysteresis during a loading–unloading cycle. The material behaviour at a strain rate of 0.01 s^{-1} is reported in **Figure S3**.
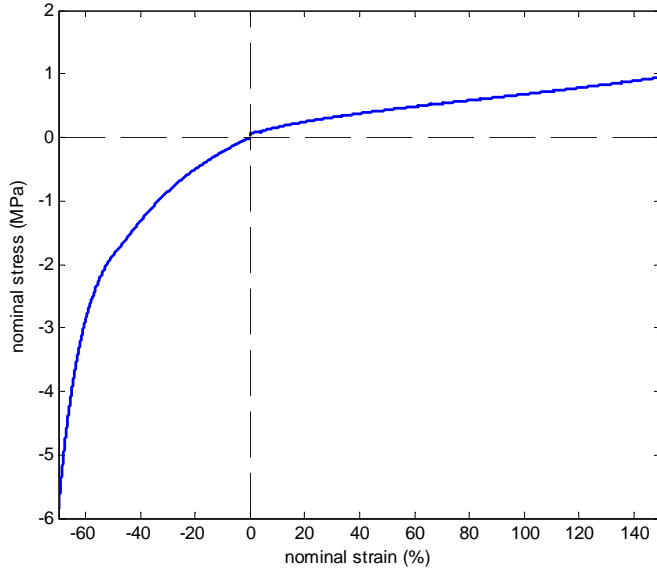
Figure S3. Experimental uniaxial stress-strain curves for P(DLLA-*co*-CL) at 0.01 s⁻¹.

2.2 Constitutive model

The observed constitutive behaviour is modelled as hyperelastic. Let $\mathbf{F} = \partial\mathbf{x}/\partial\mathbf{X}$ be the deformation gradient, mapping a material point from the reference position $\mathbf{X}$ to its current location $\mathbf{x}$ and J be its determinant, J=det($\mathbf{F}$). For an isotropic hyperelastic material the strain energy density W can be expressed as a function of the invariants of the right Cauchy-Green tensor $\mathbf{C}=\mathbf{F}^{\mathrm{T}}\mathbf{F}$ (or, alternatively, also the left Cauchy-Green tensor $\mathbf{B}=\mathbf{F}\mathbf{F}^{\mathrm{T}}$), $W = W(I_1, I_2, I_3)$, where

$$I_1 = \operatorname{tr}\mathbf{C}, \quad I_2 = \frac{1}{2}\left[\left(\operatorname{tr}\mathbf{C}\right)^2 - \operatorname{tr}\mathbf{C}^2\right], \quad I_3 = \det\mathbf{C}$$

,

I_1 being essentially a scalar equivalent stretch measure and I_3 the square of the volume ratio. Here the P(DLLA-*co*-CL) stress–strain behaviour is modelled using a Neo-Hookean model modified to include compressibility (with a high bulk modulus):

$$W(I_1, I_3) = \frac{\mu}{2}(I_1 - 3) - \mu\log J + \frac{K}{2}(J-1)^2$$

,

where μ and K are the shear and bulk modulus, respectively. The nominal stress $\mathbf{S}$ is found as

$$\mathbf{S} = \frac{\partial W}{\partial\mathbf{F}} = \mu\mathbf{F} + J\left[K(J-1) - \frac{\mu}{J}\right]\mathbf{F}^{-T}$$

.

The material was modelled as nearly incompressible, characterised by K/μ =1000. From the compression data shown in Figure S3 the initial Young's modulus was measured to be 1.35 MPa, so that μ = 1.08 MPa.

2.3 Model predictions

Figure S4 reports the experimentally observed behaviour for P(DLLA-*co*-CL)   under uniaxial tension and compression along with the model simulation of these test conditions. The constitutive model is found to accurately capture the material behaviour both under tension and compression.
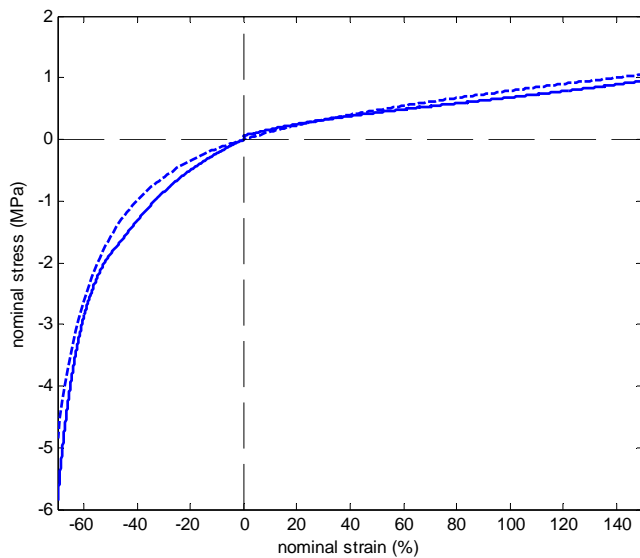

Figure S4. Nominal stress–nominal strain behaviour in uniaxial compression and tension: experimental results (continuous lines) and model prediction (dashed lines).

2.4 Numerical Simulations

Numerical simulations of the mechanical loading history of the structures were conducted utilising the nonlinear finite element code ABAQUS/Standard, version 6.6-1. Each mesh was constructed of 4-node, linear, 3-dimensional elements (ABAQUS element type C3D4). The constitutive models described above are implemented into two user material subroutine (UMAT) in the finite element software package ABAQUS and three-dimensional models of the periodic porous structures are constructed. Infinitely large structures are considered and the simulations are performed using the smallest repeating geometric unit, also referred to as representative volume element (RVE). In order to respect the periodicity of the

microstructure, a series of constraint equations are applied to the boundaries of the RVE providing general periodic boundary conditions.

3. References

[1]   Boyce MC, Parks DM, Argon AS. Large inelastic deformation of glassy-polymers .1. Rate dependent constitutive model. Mech Mater. 1988;7(1):15-33.
[2]   Bergstrom JS, Boyce MC. Constitutive modeling of the large strain time-dependent behavior of elastomers. J Mech Phys Solids. 1998;46(5):931-954.
[3]   Arruda EM, Boyce MC. A 3-dimensional constitutive model for the large stretch behavior of rubber elastic-materials. J Mech Phys Solids. 1993;41(2):389-412.